Beneficial effect of iron substitution on microstructural stability of tailored $CaTi_{0.125}Mn_{0.875-x}Fe_xTi_{0.125}O_{3-\delta}$ perovskite oxygen carrier material for chemical looping combustion

Vincent Thoréton[a], Mehdi Pishahang[b], Tommy Mokkelbost[c], Kjell Wiik[a], Yngve Larring *[b]

Abstract: $CaMn_{1-x}Ti_xO_{3-\delta}$ is the state-of-the-art perovskite-type oxygen carrier materials (OCM) used in gaseous fluidized bed chemical looping combustion (CLC) which currently undergoes upscaling and demo-campaigns in several large pilot plants around the world. The CLC application requires the control of oxygen release and uptake by the oxygen carrier material. The flexibility of the perovskite's structure allows a wide range of substitution, which can be beneficial for tuning the properties. In this study, the partial substitution of manganese by iron is investigated. The redox performances of the substituted compounds under different reducing atmospheres are discussed. During operation in a fixed bed reactor, methane conversion occurs without any soot formation. It is demonstrated that iron substitution improves the spontaneous release of oxygen, and oxygen transfer capacity of the material for moderate iron substitution close to x=0.15. Iron substitution as well effectively limits the degradation of the microstructure of the particles along redox cycling.

Introduction

Chemical looping combustion (CLC) shows great potentials as technology with high efficiency and low cost for carbon capture [1]. The CO_2 capture cost is estimated to be as low as 16-26 € per metric ton, and with an energy penalty of 4% for coal combustion [2]. Unlike other pre-combustion and post-combustion techniques, it allows the inherent separation of CO_2 during fuel combustion. Fuel combustion happens in a fuel reactor, free of nitrogen, directly with oxygen from the solid oxygen carrier material (OCM) and/or with the oxygen released by the OCM. The OCM is an oxide (normally noted as MeO), typically a transition metal oxide or a complex oxide. The spontaneous release of oxygen by the OCM, equation (1), prior to the fuel combustion, equation (2), can in the case of methane, be described by:

$$MO_{1+\delta} = MO + \frac{\delta}{2} O_2 \qquad (1)$$

$$CH_4 + 2\,O_2 = CO_2 + 2\,H_2O \qquad (2)$$

Mechanism (1–2) is commonly referred to as "chemical-looping with oxygen uncoupling" (CLOU) [3]. It is particularly beneficial in the case of solid fuel since solid-solid reaction is restricted. The direct reaction of the fuel with the OCM can be described by equation (3):

$$2\,MO_{1+\delta} + \frac{\delta}{2} CH_4 = 2\,MO + \frac{\delta}{2} CO_2 + \delta\,H_2O \qquad (3)$$

The OCM is then oxidized in an adjacent air reactor, recharging its oxygen capacity, according to equation (4):

$$MO + \frac{\delta}{2} O_2 = MO_{1+\delta} \qquad (4)$$

The release of oxygen from an OCM is therefore an important factor to control in CLC. For instance, too early release of oxygen in the loop-seal (the chamber filled with steam separating the air and fuel reactors) should be limited and oxygen should be released as quickly as possible in the fuel reactor of a circulating fluidized bed (CFB) CLC. This aspect is even more critical in the case of fixed bed CLC, where the oxygen release during inert flushing should be prevented [4]. In addition to kinetics, OCM must retain several qualities along reduction/oxidation (redox) cycles such as high oxygen capacity, high redox kinetics, good mechanical properties *i.e.* low fragmentation, attrition and agglomeration. Furthermore, materials must be of low cost and low toxicity [5]. From expensive nickel oxide to low cost ores [6, 7, 8], several hundreds of materials based on Ni, Cu, Fe, Mn, Co and mixture of these have been studied as potential OCM for CLC [9]. Lately, a significant interest has been shown towards mixed transition metal oxides [10], and complex perovskite-type oxides [11] especially those derived from the calcium manganite $CaMnO_{3-\delta}$ family. For CLC application, substitution of the calcium by strontium and barium [12] were considered. Furthermore, the substitution of manganese by magnesium [13], titanium [4, 14] or a combination of both [15] have been investigated. Substantial improvement from iron substitution were reported [16, 17]. $CaMn_{1-x}Ti_xO_{3-\delta}$ has proven to have high activity with respect to CH_4 reduction [18]. Stability of the perovskite structure is shown to be enhanced by Ti substitution [4, 14], reflecting the higher enthalpy of formation (stability) of $CaTiO_3$ compared to $CaMnO_3$ [19]. It has been demonstrated that $CaMn_{0.875}Ti_{0.125}O_{3-\delta}$ shows promising performance as an OCM with its spontaneous oxygen release [20]. Furthermore it has been shown that it has good chemical stability and shows small dimensional changes upon redox cycling [21]. It is also observed that the re-oxidation is faster for Ti-substituted $CaMnO_3$ at high temperatures [16], and Ti doping

[a] Department of Materials Science and Engineering, NTNU, Norwegian University of Science and Technology, Trondheim, Norway
[b] SINTEF Materials and Chemistry, P.O. Box 124 Blindern, NO-0314 Oslo Norway
[c] SINTEF Materials and Chemistry, NO-7465 Trondheim, Norway

Corresponding Author:
Yngve Larring, SINTEF Materials and Chemistry, Sustainable Energy Technology, P.O. Box 124 Blindern, NO-0314, Oslo, Norway. E-mail: Yngve.Larring@sintef.no; Fax: +47 2206 7350; Tel: +47 9828 3956.

positively influences the reduction reaction rate and broadened the operation window of the oxygen carrier material (OCM) to lower temperatures [22].

In this article, the effect of iron substitution on the stoichiometric perovskite $CaMn_{0.875-x}Fe_xTi_{0.125}O_{3-\delta}$ is investigated. The evolution of lattice parameters is followed as a function of iron content. The phase stability is checked and the total oxygen capacity is determined. Reducing and oxidizing rates are measured by cyclic thermogravimetric measurements (TG) under reducing and oxidizing atmospheres (redox), imitating the conditions under CLC operation. The spontaneous release of oxygen from the material and conversion of CH_4 are quantified and discussed. The evolution of the microstructure of particles is investigated. The possible use of this system as an OCM for CFB CLC is also discussed.

.

Results and Discussion

Samples synthesis and characterizations

XRD diffractograms recorded on the CMTF fine powder (fraction sieved under 45 microns) were refined in the orthorhombic Pnma space group showing that single-phase perovskite structures were obtained at room temperature (see appendix 1). Lattice parameters (a, $\sqrt{2}\cdot$b, and c) as a function of the iron content are shown in Figure 1 as well as the relative density of the tablets after sintering. Lattice parameters increase almost linearly with the fraction of Fe substituting the Mn site following Vegard's law[21]. This is believed to be helpful to the oxygen mobility in the lattice, and as well to ease the strain between the grains. The relative density increases with iron substitution. This gain in density should be beneficial to OCM's mechanical properties.

Phase stability under inert and reducing conditions and oxygen capacity

During CLC operation, the OCM is reduced and oxidized in a cyclic way. Bakken *et al.* have shown that $CaMnO_3$ transforms into Ca_2MnO_4 and $CaMn_2O_4$ under reducing conditions [23]. It has been assumed that titanium substitution prevents to some extent this transformation [14, 20]. Here, we followed the phase transitions of CMT and CMTF under inert and mild reducing atmospheres. Under N_2, the in-situ XRD experiment at 800˚C showed that the perovskite structure is retained with only a slight but quick shift of the cell parameters, as illustrated in Figure 2. This is in good agreement with the lattice expansion induced by the loss of oxygen and with the flexibility of the oxygen stoichiometry possibly ranging from 2.5 to 3 in the perovskite structure [24, 25]. On the other hand, the phase analysis by XRD (Figure 3) and the thermogravimetric measurement (Figure 4 (a)) indicate that the long-term exposure to 5% H_2 leads to the full dissociative reduction, in other words the material conversion, of the initial $CaMn_{0.875-x}Fe_xTi_{0.125}O_{3-\delta}$ perovskite to $Ca_{0.5}(Mn,Fe)_{0.5}O$ rock-salt and $CaTiO_3$ perovskite. Besides, the in-situ XRD experiment at 800˚C confirmed a quick phase transition under reducing conditions (not shown). Higher temperature allowed the complete recombination to the original perovskite under oxidizing conditions.. Higher temperature allowed complete recombination to the original perovskite. It should be noted that the XRD analyses only applies to the surface of the material that is in direct contact with the surrounding atmosphere. In the case of oxygen carrier particles in the range of 90-125µm, the phase transition is limited by the oxygen diffusion in the bulk. Indeed, the observed phase transformation does not reflect fluidized bed conditions we aim at since the material will never release its full oxygen capacity in the CFB application. The total oxygen capacity however can be used as an indication to normalize the material conversion during the redox cycling. We define the total oxygen capacity as the amount of oxygen that a freshly made material release according to its full dissociative reduction. As shown in Figure 4 (b), the total oxygen capacity decreases proportionally with the iron content. This observation is consistent with the lower availability of reducible Mn^{4+} caused by the iron substitution.

Conversion activity & Chemical Looping Oxygen Uncoupling

We investigated the release of oxygen (CLOU) under inert atmosphere and the conversion of methane using a TPX setup. In this experiment, 0.5g of the material acts as an oxygen buffer. The response of a gas flow was analyzed by mass spectrometry at the outlet of the reactor. Figure 5 presents the concentration profile of N_2, O_2, CH_4, CO_2 and CO along the experiment performed on CMT at 950˚C. In the first part (up to 45 minutes), the fully oxidized material releases its oxygen in He inert atmosphere and then is re-oxidized. In the second part, up to 85 minutes, the feeding gas flow is switched from 5% O_2 to He (30 min) then to 10% CH_4 (5 min).

Spontaneous oxygen release under inert atmosphere

As shown in the in-situ XRD, the perovskite retains its structure under an inert atmosphere (Figure 2). Figure 6 presents the oxygen release in an inert flow (He) for CMT, CMTF15 and CMTF20 from 950 to 800 ºC. At 950 ºC (Figure 6 (a)) and 900 ºC (Figure 6 (b)) the spontaneous release of oxygen is driven by thermodynamic factors. However, at 850 ºC (Figure 6 (c)) and 800 ºC (Figure 6 (d)), the exchange kinetics of oxygen decline (a smaller amount of oxygen is released), showing a clear advantage to the materials doped with iron. Figure 7 summarizes the amount of oxygen released after 30 minutes as a function of temperature for different compositions. This demonstrates that the total capacity of the material is not so crucial. Indeed, the efficiency/kinetics of release are more important especially at the lowest temperatures. Iron doped compounds should have an advantage for the application since the oxygen transfer will be facilitated earlier during start up while the system is heated up.

CLOU

The conversion experiments' results are more of qualitative nature. As illustrated respectively in Figure 5 (right part) and Figure 8 (a) at 950˚C, CMT and CMTF15 give a full conversion nearly for three minutes before a breakthrough of CH_4 happens, while CO level remains very low. The same behavior is observed for all the samples, except that the total amount of oxygen released by the oxygen carrier decreases with the iron substitution and therefore the amount of CH_4 converted. This is

consistent with the decreasing oxygen capacity. At lower temperature, the breakthrough of CH_4 starts earlier, showing that the conversion is limited by the oxygen release kinetics, as illustrated on Figure 8, from 950 ˚C (a) to 800 ˚C (d).

H_2 and CH_4 redox cycling and kinetics

Along redox cycling measurements in a thermogravimetric analyzer, CMTF samples were exposed to sequential reducing and oxidizing atmospheres with quick gas switching (2 minutes exposures). Given the very short exposure time, the thermodynamic equilibrium is never reached. Although simplistic, this procedure provides a methodology to analyze the OCMs performance, during and after a large number of redox cycles, similar to those under CFB CLC. The chosen reducing atmospheres (respectively with 10% CH_4 and with 5% H_2) simulate the extremal reducing conditions in the fuel reactor, from harsh reducing conditions (simulating the fuel reactor's inlet) to mild reducing conditions (simulating the fuel reactor's outlet). All along the cycles, the $p(O_2)$ stayed high enough to avoid the full reduction to elemental iron. The redox cycles series at 950 ˚C under H_2 and CH_4 are respectively shown in Figure 9 (a) and (b). The material conversion is normalized to the total oxygen capacity. Initially, the material is fully oxidized in air; *i.e.* the initial normalized material conversion is at 0%. Materials' conversion at 100% corresponds to the full release of its total oxygen capacity. For all compositions, it took two cycles for the material and the instrumental setup to reach a new dynamic equilibrium. The reduction and oxidation reaction rates were derived from the maximum tangent slope of the following cycles as detailed before [7, 8]. Those are reported in Figure 10.

Remarkably, the response to the atmosphere changes are notably shortened for the samples containing iron. The spontaneous release of oxygen (*i.e.* the CLOU effect) is particularly favored by the iron substitution under the inert atmosphere as shown in Figure 10 (a) (plain lines). In addition, the oxygen release rate under mild reducing conditions increases with the iron content (up to 15%) as shown in Figure 10 (a) (dashed lines). On the other hand, under harsh reducing conditions, *i.e.* along CH_4 redox cycling, iron substitution has no influence on the oxygen release rate (up to 15%), which is as expected significantly higher to the one under H_2 redox cycling (Figure 10 (a), dotted lines). The re-oxidation kinetics along the H_2 cycling are promoted by the iron substitution as shown in Figure 10 (b). They are very similar to those along CH_4 cycling (not shown).

The oxygen capacity values at different conditions are summarized in Figure 11. Overall, from green dashed line one can clearly notice that the amplitude of the material conversion under H_2 redox cycling increases with the iron content up to 15%, even if the oxygen capacity (green plain line) decreases. Practically, it allows using the oxygen capacity more efficiently. In addition, having an OCM with improved oxygen release in mild reducing conditions is particularly beneficial in order to improve fuel's conversion at the outlet of the fuel reactor. The CLOU capacity, determined from the TPX measurement under inert atmosphere, is also reported (black discs). Overall, the perovskite structure releases a fairly large amount of oxygen under a flow of inert gas, *i.e.* up to almost $5\%_m$ at 950˚C for CMT. Optimal redox kinetics are observed with an iron content close to 15%. However, increasing further the iron content to 20% is less beneficial to the redox kinetics. This is consistent with the results obtained from the oxygen release in inert experiments performed by TPX (see Figure 6).

The beneficial effects provided by the iron substitution could be the result of an improvement of the surface kinetics provided by the additional electronic conductivity and higher amount of oxygen defects as proposed by Galinsky *et al.* [26] on iron based OCM supported on lanthanum strontium ferrite (LSF). Singh showed that higher iron substitution on calcium manganite reduces both the electronic conductivity and the oxygen defects concentration with the formation of Fe^{4+} [27]. The earlier release of oxygen is therefore possibly due to a lower thermodynamic stability induced by iron substitution. The clear improvements observed at relatively low temperature (800˚C), must be closely related to oxygen mobility improvements caused by the structural modification and increased lattice parameters (see Figure 1) as well as improved oxygen exchange kinetics at the surface, which we will characterize in a future study.

Evolution of redox kinetics and post-analysis

No evolution of redox rates was observed under H_2 cycling, showing that the dynamic cycling under mild reducing conditions is a reversible process with no sign of deterioration. However, it was noticeable that reduction rates and the material conversion amplitude under CH_4 increases slightly along the cycles, and this is valid at higher extents for CMT. This is attributed to a microstructural change of the material during the redox cycles; this is most likely related to an increase of the surface area going along with the sequential partial phase separation and regeneration of the material. This is consistent with the evolution of the microstructure shown in Figure 12. It shows that the microstructure of CMT is subject to swelling and disintegration after the short cycling experiments in harsh reducing conditions. This is clearly restricted by introduction of iron into the structure. This indicates that cation diffusion is further restricted in this structure compared to the CMT sample without iron. This is in good agreement with the post-mortem XRD analysis showing that the materials, cooled down under oxidizing atmosphere, are partially amorphous with the presence of a spinel phase and two perovskite phase. Cell parameters of three phases are respectively close to those of $CaMn_2O_4$ spinel, $CaTiO_3$ perovskite and the original CMTF perovskite. This is shown in Figure 13. After the fast cooling of the samples in air, the CMFT15 sample contains for the most part the initial perovskite phase. This supports the faster recombination to a perovskite structure compared to CMT, in which a large portion of the initial perovskite structure is not reformed.

Conclusions

In this study, we systematically followed the oxygen release from $CaMn_{0.875-x}Fe_xTi_{0.125}O_{3-\delta}$ under inert atmosphere and extremal reducing conditions. Iron substitution on the Mn site of the CMT perovskite steadily improves the oxygen release rates under

inert atmosphere *i.e.* the CLOU effect, particularly at lower temperatures. The fuel conversion is supported as well under mild reducing conditions. This should assist the conversion of residual fuel at the outlet of the fuel reactor, thus improves the overall fuel conversion. The optimum performance is obtained with 15% substitution of Mn by Fe. Furthermore, the iron substitution is highly beneficial to retain the material's microstructure by accelerating the recombination to the perovskite phase during the re-oxidation step.

Experimental Section

Materials synthesis

Five compositions with increasing iron content of the stoichiometric $CaMn_{0.875-x}Fe_xTi_{0.125}O_{3-\delta}$ perovskites (CMTF) were synthesized by solid-state reaction. The samples are respectively named CMT ($CaMn_{0.875}Ti_{0.125}O_{3-\delta}$), CMTF05 ($CaMn_{0.825}Fe_{0.05}Ti_{0.125}O_{3-\delta}$), CMTF10 ($CaMn_{0.775}Fe_{0.10}Ti_{0.125}O_{3-\delta}$), CMTF15 ($CaMn_{0.725}Fe_{0.15}Ti_{0.125}O_{3-\delta}$) and CMTF20 ($CaMn_{0.675}Fe_{0.20}Ti_{0.125}O_{3-\delta}$). All the samples were prepared from $CaCO_3$ (Sigma–Aldrich, >99.95%), Mn_2O_3 (Aldrich, >99%), Fe_2O_3 (Aldrich, >99.995%) and TiO_2 (Merck, >99%). For each composition, the reactants were intimately ground by hand in an agate mortar. A tablet (15 mm Ø) was prepared by uniaxial pressing (30 MPa). To ensure complete and homogeneous reaction it was annealed for 6 hours in air up to 1260 °C, with intermediate grindings. Density was measured by the buoyancy method. The tablet was crushed and sieved for further characterizations.

Characterizations

Ambient temperature X-ray diffraction (XRD) was performed on a Bruker Da Vinci diffractometer with a LinxExe XE detector using CuKα radiation accelerated at 40 kV and 40 mA. Finely crushed powder was used, and data was collected from 15° to 75° with a step size of 0.013° and 1 second counting time. Fullprof v5.30 software was used to refine the XRD data [28]. Peaks were fit with a Pseudo-Voigt profile function. The displacement, cell parameters and Pseudo-Voigt parameters (U,V,W, shape) were refined. In-situ X-Ray diffraction measurements were carried out using a D8 Advance diffractometer using a Pt strip type resistive heater. The fast acquisition was performed using a fixed PSD Vantec detector in the 30˚-36˚ angular window (2θ). The flow in the chamber was controlled with a mechanical flow meter using synthetic air or nitrogen. Scanning electron microscopy (SEM) was performed using a Hitachi S-3400N microscope equipped with an EDS Oxford X-Max detector.

Thermogravimetric analysis were performed using a modified Setaram Setsys Evolution apparatus. A YSZ based electrochemical oxygen sensor supplied by ECONOX was implanted into the TGA, with its measuring point just 10 mm below the sample. A constant reactive gas flow was set to 200 mL/min, from bottom to the top. This helps to minimize the convection effect and provides more stable gravimetric data. Platinum wire and platinum crucible were used to suspend the sample in the apparatus. Blank experiments were performed to correct the data from the experimental background. Redox cycling measurements were performed on freshly sieved (90-125µm) 40±5mg samples. The procedure is similar to the one described by Fossdal *et al.* [7] and Larring *et al.* [8]. The reducing conditions were adjusted with 2% steam (Steam Methane Reforming/Water Gas Shift reactions) and 25% CO_2 (Dry Reforming). Under oxidizing conditions, CO_2 works as an inert gas. This procedure is actually not a verification of the CLC but is designed to simulate the frequent and sharp redox cycles that the OCM will undergo during the circulating fluidized bed CLC operation. It involves series of 20 redox cycles with 2 minutes reducing and oxidizing steps, with an inert step of 2 minutes in between. In those conditions, the thermodynamic is never reached. Each series is followed by a re-oxidation stage (30 minutes) in order to re-equilibrate the materials' oxygen content. Series are repeated at five different temperatures (800˚C, 850˚C, 900˚C, 950˚C and 1000˚C then back to 800˚C) under mild reducing conditions (5% H_2, 25% CO_2 and 2% H_2O in Ar) or harsh reducing conditions (10% CH_4, 25% CO_2 and 2% H_2O in Ar). Oxidizing atmosphere is 20% O_2, 25% CO_2 and 2% H_2O in Ar. In total, the procedure consists of 240 redox cycles. The samples were cooled down (10 K/min) in air at the end of the thermogravimetric experiments. The oxygen capacity of the materials was also determined by reducing fresh samples for a long time (2 hours) until the thermodynamic equilibrium, under the same gas conditions at 800, 900 and 1000˚C. The conversion measurements were performed from 800˚C to 950˚C with 50˚C incremental steps using a TPX setup (MICROMERITICS AutoChem 2910 TPX apparatus and VG ProLab 1-300 amu MS). Sieved material in the range of 125–180 µm was used and 0.5±0.01 g of sample was used in each TPX experiment. The gas flow (30mL/min) was successively set from oxidizing (5% O_2 + 5% N_2 in He for 60 minutes) to inert (He for 30 minutes) and from oxidizing (60 min) to reducing conditions (10% CH_4 in He for 5 minutes). The composition of the outlet gas was followed by MS in order to study the CLOU effect as well as the conversion respectively. The gas mixtures used in the atmospheric experiments (TGA and TPX) are summarized in Table 1.

Acknowledgements

This work forms part of the BIGCLC Phase III project supported by the Research Council of Norway (id 224866 and id 193816). The work has additionally been produced with support from the BIGCCS Centre, performed under the Norwegian research program Centers for Environment-friendly Energy Research (FME). The authors acknowledge the following partners for their contributions: Aker Solutions, Gassco, Shell, Statoil, TOTAL, GDF SUEZ and the Research Council of Norway.

Keywords: calcium manganite, oxygen release, CLC, CLOU, CMT, CMTF, TPX.

References

1. M. E. Boot-Handford, J. C. Abanades, E. J. Anthony, M. J. Blunt, S. Brandani, N. Mac Dowell, J. R. Fernández, M.-C. Ferrari, R. Gross, J. P. Hallett, R. S. Haszeldine, P. Heptonstall, A. Lyngfelt, Z. Makuch, E. Mangano, R. T. J. Porter, M. Pourkashanian, G. T. Rochelle, N. Shah, J. G. Yao, and P. S. Fennell, "Carbon capture and storage update," *Energy & Environmental Science,* 7[1] 130 (2014).
2. A. Lyngfelt and B. Leckner, "A 1000 MWth boiler for chemical-looping combustion of solid fuels – Discussion of design and costs," *Applied Energy*.
3. T. Mattisson, A. Lyngfelt, and H. Leion, "Chemical-looping with oxygen uncoupling for combustion of solid fuels," *International Journal of Greenhouse Gas Control,* 3[1] 11-19 (2009).
4. M. Pishahang, Y. Larring, M. McCann, and R. Bredesen, "$Ca_{0.9}Mn_{0.5}Ti_{0.5}O_{3-\delta}$: A Suitable Oxygen Carrier Material for Fixed-Bed Chemical Looping Combustion under Syngas Conditions," *Industrial & Engineering Chemistry Research,* 53[26] 10549-56 (2014).
5. A. Lyngfelt, "Chemical-looping combustion of solid fuels – Status of development," *Applied Energy,* 113[0] 1869-73 (2014).
6. H. Leion, T. Mattisson, and A. Lyngfelt, "Use of Ores and Industrial Products As Oxygen Carriers in Chemical-Looping Combustion," *Energy & Fuels,* 23[4] 2307-15 (2009).
7. A. Fossdal, E. Bakken, B. A. Øye, C. Schøning, I. Kaus, T. Mokkelbost, and Y. Larring, "Study of inexpensive oxygen carriers for chemical looping combustion," *International Journal of Greenhouse Gas Control,* 5[3] 483-88 (2011).
8. Y. Larring, M. Pishahang, M. F. Sunding, and K. Tsakalakis, "Fe–Mn based minerals with remarkable redox characteristics for chemical looping combustion," *Fuel,* 159 169-78 (2015).
9. M. Rad, Imanieh, M. & Nadarajah, A. , "Perovskite ceramics and recent experimental progress in reactor design for chemical looping combustion application. ," *Chemical Papers,* 69[5] 22 (2015).
10. Y. Larring, C. Braley, M. Pishahang, K. A. Andreassen, and R. Bredesen, "Evaluation of a Mixed Fe–Mn Oxide System for Chemical Looping Combustion," *Energy & Fuels,* 29[5] 3438-45 (2015).
11. J. C. Abanades, B. Arias, A. Lyngfelt, T. Mattisson, D. E. Wiley, H. Li, M. T. Ho, E. Mangano, and S. Brandani, "Emerging CO_2 capture systems," *International Journal of Greenhouse Gas Control*.
12. N. Galinsky, A. Mishra, J. Zhang, and F. Li, "$Ca_{1-x}A_xMnO_3$ (A = Sr and Ba) perovskite based oxygen carriers for chemical looping with oxygen uncoupling (CLOU)," *Applied Energy,* 157 358-67 (2015).
13. A. Cabello, A. Abad, P. Gayán, L. F. de Diego, F. García-Labiano, and J. Adánez, "Effect of Operating Conditions and H2S Presence on the Performance of $CaMg_{0.1}Mn_{0.9}O_{3-\delta}$ Perovskite Material in Chemical Looping Combustion (CLC)," *Energy & Fuels,* 28[2] 1262-74 (2014).
14. H. Leion, Y. Larring, E. Bakken, R. Bredesen, T. Mattisson, and A. Lyngfelt, "Use of $CaMn_{0.875}Ti_{0.125}O_3$ as Oxygen Carrier in Chemical-Looping with Oxygen Uncoupling," *Energy & Fuels,* 23[10] 5276-83 (2009).
15. A. Abad, F. García-Labiano, P. Gayán, L. F. de Diego, and J. Adánez, "Redox Kinetics of $CaMg_{0.1}Ti_{0.125}Mn_{0.775}O_{2.9-\delta}$ for Chemical Looping Combustion (CLC) and Chemical Looping with Oxygen Uncoupling (CLOU)," *Chemical Engineering Journal*[0].
16. P. Hallberg, D. Jing, M. Rydén, T. Mattisson, and A. Lyngfelt, "Chemical looping combustion and chemical looping with oxygen uncoupling experiments in a batch reactor using spray-dried $CaMn_{1-x}M_xO_{3-\delta}$ (M = Ti, Fe, Mg) particles as oxygen carriers," *Energy and Fuels,* 27[3] 1473-81 (2013).
17. N. Galinsky, M. Sendi, L. Bowers, and F. Li, "CaMn1−xBxO3−δ (B = Al, V, Fe, Co, and Ni) perovskite based oxygen carriers for chemical looping with oxygen uncoupling (CLOU)," *Applied Energy,* 174 80-87 (2016).
18. H. Taguchi, K. Nakade, M. Yosinaga, M. Kato, and K. Hirota, "Methane Oxidation on Perovskite-Type $Ca(Mn_{1-x}Ti_x)O_{3-\delta}$," *Journal of the American Ceramic Society,* 91[1] 308-10 (2007).
19. S. Stølen and T. Grande, "Trends in Enthalpy of Formation," pp. 197-227. in Chemical Thermodynamics of Materials**.** John Wiley & Sons, Ltd, 2004.
20. M. Rydén, A. Lyngfelt, and T. Mattisson, "$CaMn_{0.875}Ti_{0.125}O_3$ as oxygen carrier for chemical-looping combustion with oxygen uncoupling (CLOU)—Experiments in a continuously operating fluidized-bed reactor system," *International Journal of Greenhouse Gas Control,* 5[2] 356-66 (2011).
21. A. Fossdal, O. Darell, A. Lambert, E. Schols, E. Comte, R. Leenman, and R. Blom, "Study of dimensional changes during redox cycling of oxygen carrier materials for chemical looping combustion," *Energy and Fuels,* 29[1] 314-20 (2015).
22. M. Pishahang, Y. Larring, M. Sunding, M. Jacobs, and F. Snijkers, "Performance of Perovskite-Type Oxides as Oxygen-Carrier Materials for Chemical Looping Combustion in the Presence of H_2S," *Energy Technology,* 4[10] 1305-16 (2016).

23. E. Bakken, T. Norby, and S. Stolen, "Nonstoichiometry and reductive decomposition of CaMnO," *Solid State Ionics,* 176[1-2] 217-23 (2005).
24. J. M. D. Coey, M. Viret, and S. von Molnár, "Mixed-valence manganites," *Advances in Physics,* 48[2] 167-293 (1999).
25. E. Girdauskaite, H. Ullmann, M. Al Daroukh, V. Vashook, M. Bülow, and U. Guth, "Oxygen stoichiometry, unit cell volume, and thermodynamic quantities of perovskite-type oxides," *Journal of Solid State Electrochemistry,* 11[4] 469-77 (2007).
26. N. L. Galinsky, Y. Huang, A. Shafiefarhood, and F. Li, "Iron Oxide with Facilitated O^{2-} Transport for Facile Fuel Oxidation and CO_2 Capture in a Chemical Looping Scheme," *ACS Sustainable Chemistry & Engineering,* 1[3] 364-73 (2013).
27. B. Singh, "Structural, transport, magnetic and magnetoelectric properties of $CaMn_{1-x}Fe_xO_3$-[small delta] (0.0 [less-than-or-equal] x [less-than-or-equal] 0.4)," *RSC Advances,* 5[50] 39938-45 (2015).
28. J. Rodríguez-Carvajal, "Recent advances in magnetic structure determination by neutron powder diffraction," *Physica B: Condensed Matter,* 192[1] 55-69 (1993).

Tables

Table 1: Gas mixtures used in the atmospheric experiments. TGA and TPX experiments are detailed.

TGA redox cycles (from 800 to 1000 °C with 50 °C steps)									
	Step	Gas Type	Time at Setpoint (minutes)	Gas Concentration (vol%)					
				H_2	CH_4	CO_2	H_20	Ar	O_2
H_2 short redox cycles (20 cycles)	1	Oxidizing	2	–	–	25	2	53	20
	2	Inert	2	–	–	25	2	73	–
	3	Reducing	2	5	–	25	2	68	–
	4	Inert	2	–	–	25	2	73	–
CH_4 short redox cycles (20 cycles)	1	Oxidizing	2	–	–	25	2	53	20
	2	Inert	2	–	–	25	2	73	–
	3	Reducing	2	–	10	25	2	63	–
	4	Inert	2	–	–	25	2	73	–

TGA long redox cycles (from 800 to 1000 °C with 100 °C steps)									
H_2 long redox cycles	1	Oxidizing	30	–	–	25	2	53	20
	2	Inert	5	–	–	25	2	73	–
	3	Reducing	120	5	–	25	2	68	–
	4	Inert	5	–	–	25	2	73	–

TPX cycles (800˚C to 950˚C with 50˚C steps)									
	Step	Gas Type	Time at Setpoint (minutes)	Gas Concentration (vol%)					
				H_2	CH_4	N_2	H_20	He	O_2
Spontaneous oxygen release	1	Oxidizing	60	–	–	5	–	90	5
	2	Inert	30	–	–	0	–	100	–
Conversion activity	1	Oxidizing	60	–	–	5	–	75	20
	2	Reducing	5	–	10	–	–	90	–
	3	Inert	5	–	–	0	–	100	–

Figures

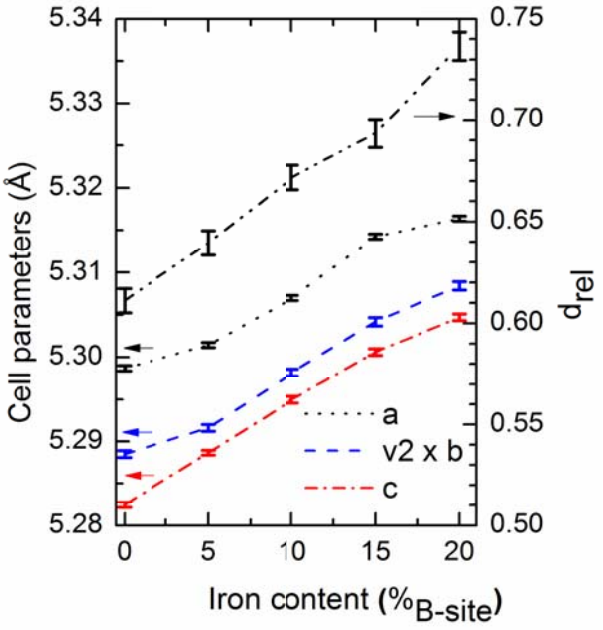

Figure 1. Cell parameters and relative density of the tablets after sintering, as a function of iron content.

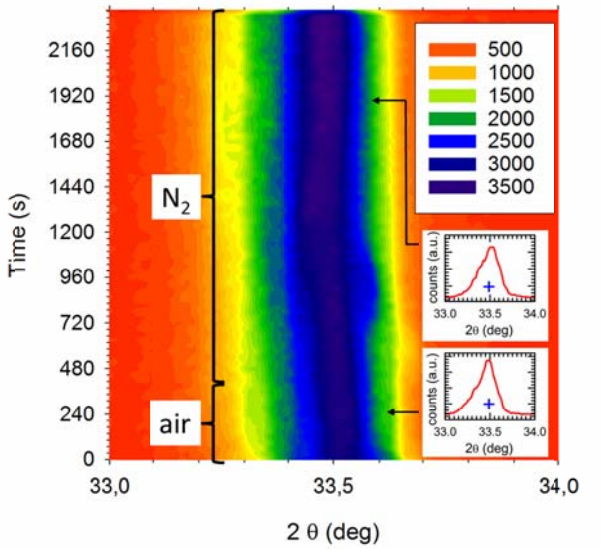

Figure 2. Details of the X-Ray diffraction fast acquisition (30 seconds per scan) at 800˚C on CMTF15. The atmosphere is switched from synthetic air to N_2. The blue plus markers in the sub-figures at 33.5 indicate were the perovskite peak is expected.

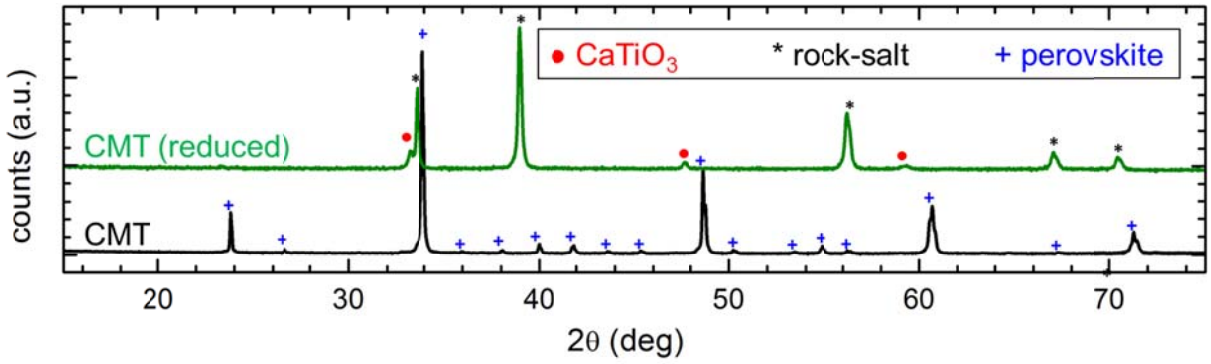

Figure 3. X-Ray diffractogram of CMT after reduction under 5% H_2 at 1000˚C. The diffractogram of the original perovskite is displayed for comparison.

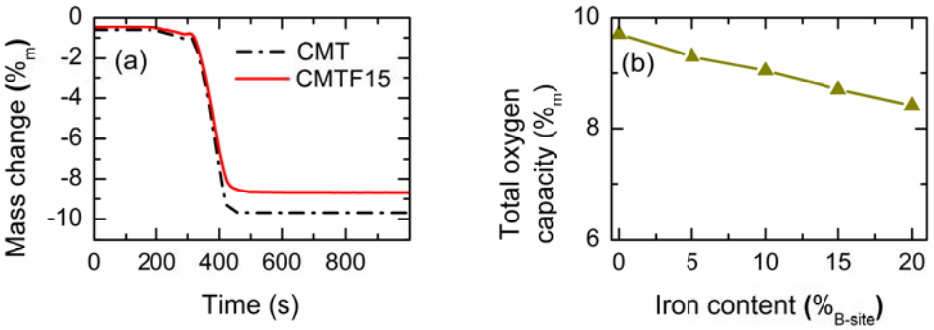

Figure 4. (a) Example of the thermogravimetric data recorded on oxidized samples of CMT and CMTF15 during the long-term exposure to the mild reducing atmosphere at 1000˚C. (b) Total oxygen capacity as a function of the iron content.

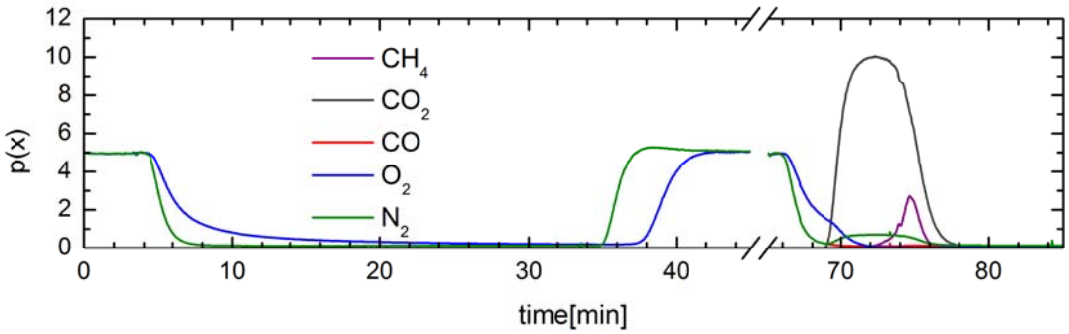

Figure 5. Concentration profile of O_2, N_2, CH_4, CO_2 and CO as a function of time at the outlet of the TPX reactor filled with CMT at 950˚C.

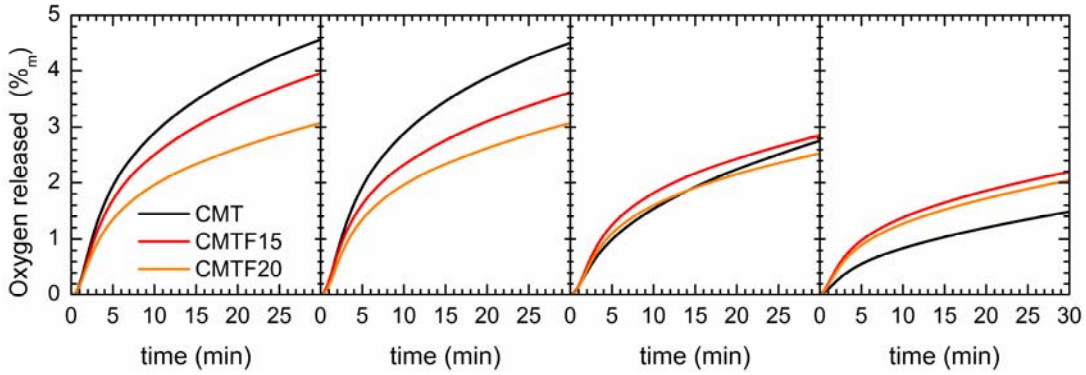

Figure 6. Total amount of oxygen released by TPX in function of time under a flow of He from 950 ºC to 800 ºC for oxidized samples of CMT (black curve), CMTF15 (red curve) and CMTF20 (orange curve).

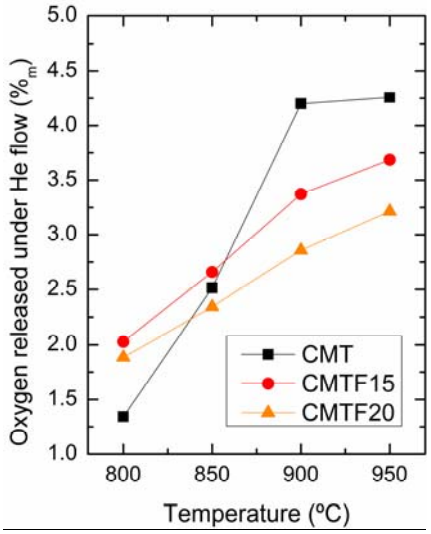

Figure 7. Oxygen released from oxidized samples after 30 minutes in the TPX experiment under a flow of inert gas as a function of temperature for CMT (black squares), CMTF15 (red discs) and CMTF20 (orange triangles).

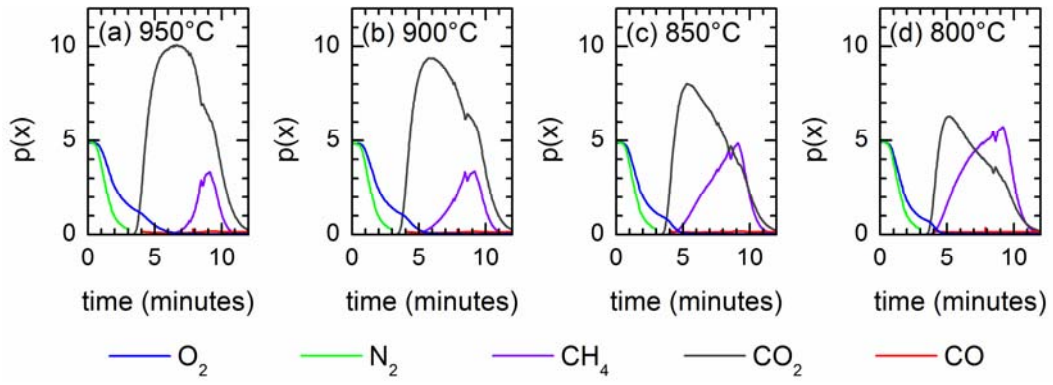

Figure 8. Concentration profile of O_2, N_2, CH_4, CO_2 and CO as a function of time at the outlet of the TPX reactor filled with CMTF15 from 800 to 950 ˚C.

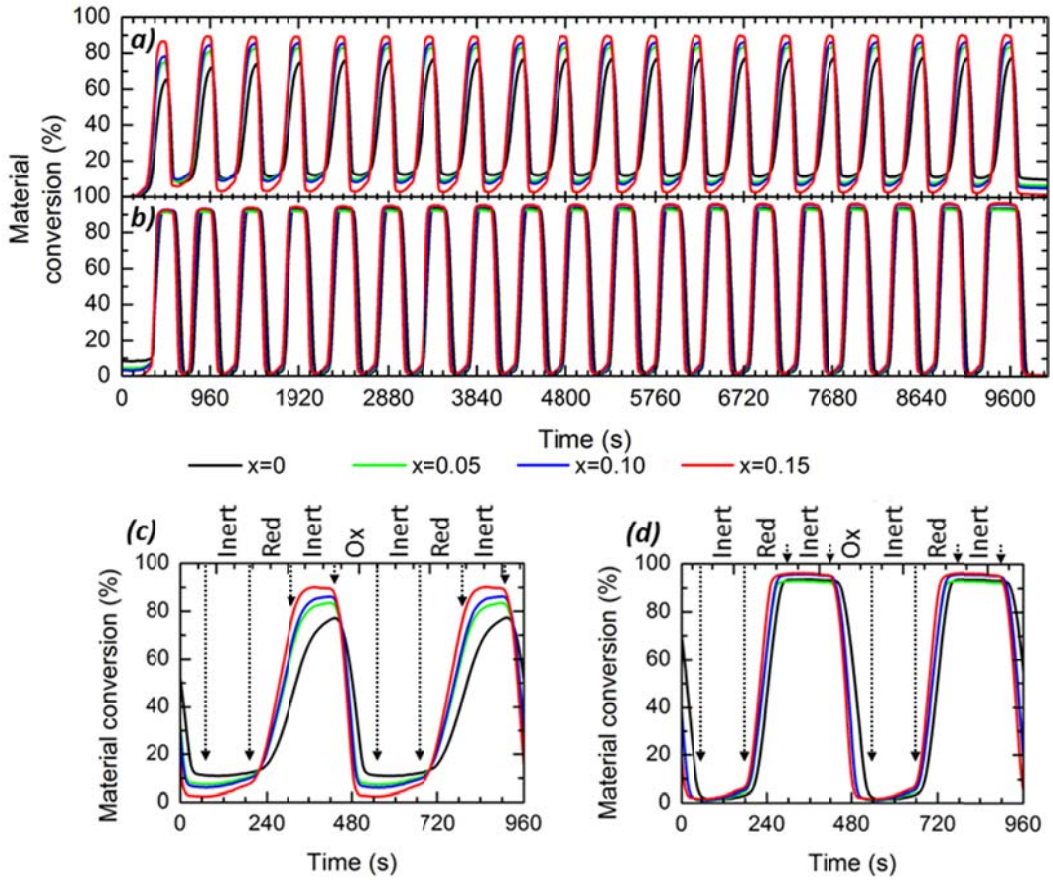

33

34 Figure 9. Material conversion at 950˚C along H_2 (a) and CH_4 (b) short redox cycling for $CaMn_{0.875-x}Fe_xTi_{0.125}O_{3-\delta}$.
35 Magnifications over 2 cycles are shown respectively in (c) and (d). The curves were synchronized when the TGA
36 valve switches at the initial oxidizing step. For the figure clarity, only the material conversion of CMT (black),
37 CMTF05 (green), CMTF10 (blue) and CMTF15 (red) are displayed.

38

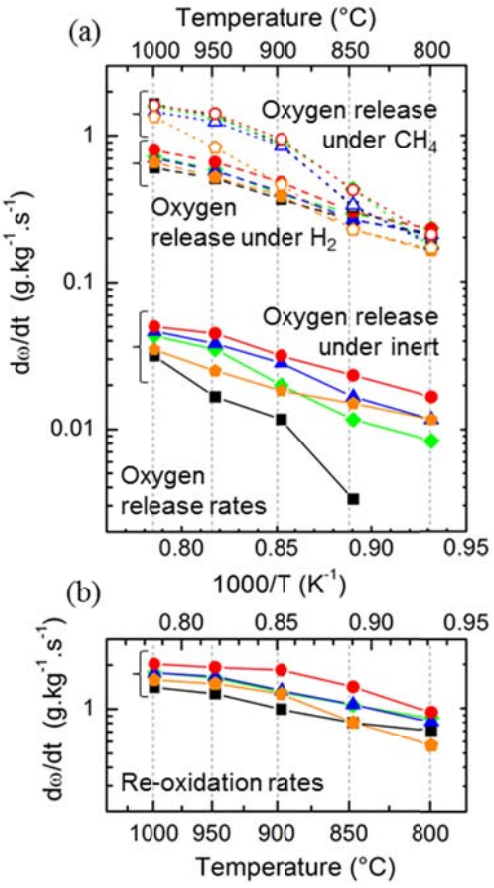

Figure 10. (a) Oxygen release rates under inert atmosphere (plain lines), 5% H_2 reducing atmosphere (dashed lines) and 10% CH_4 reducing atmosphere (dotted lines and empty symbols). (b) Re-oxidation rates during the H_2 redox cycling. CMT (black), CMTF05 (green), CMTF10 (blue), CMTF15 (red) and CMTF20 (orange). Those measurements were performed by TGA.

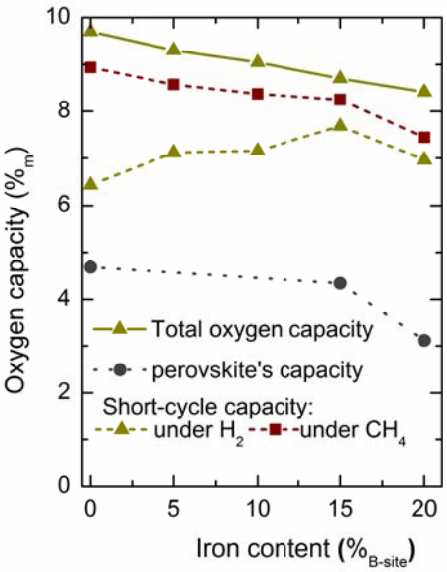

Figure 11. Effect of iron content on the total oxygen capacity (plain line), the CLOU capacity (from TPX) at 950˚C (dotted line) and the conversion amplitude under TGA redox cycling (dashed lines) at 950˚C under 5 % H_2 (green) and 10% CH_4 (red).

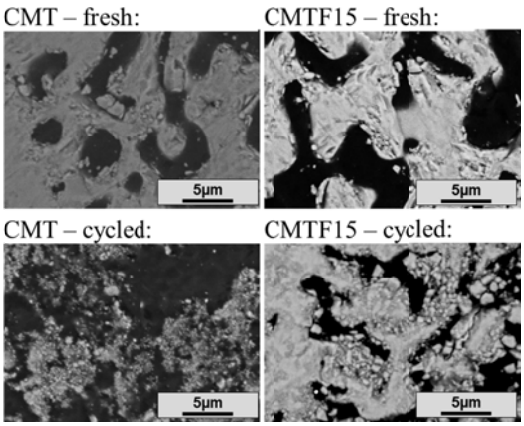

Figure 12. SEM micrographs of cross-sections of OCM particles before and after short redox cycling.

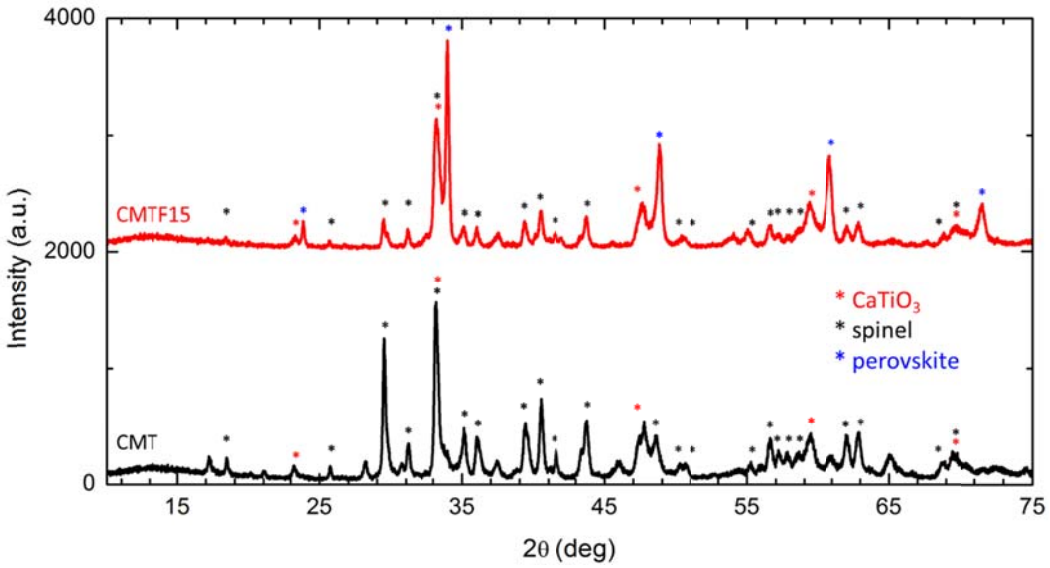

Figure 13. X-Ray diffractograms of CMT and CMTF15 after the 240 redox cycles in the thermogravimetric analyser.

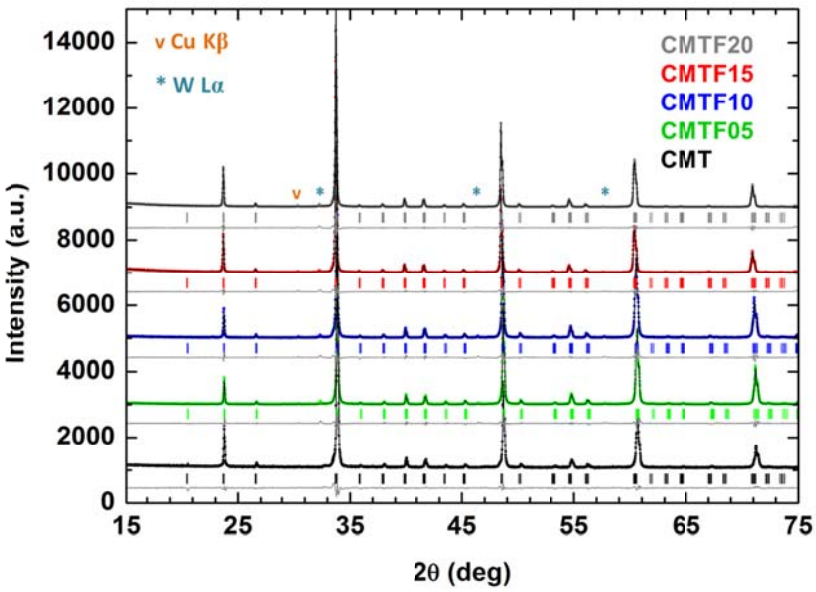

55 ➢

56 Appendix 14. X-Ray data (dots) and corresponding profile refinements (lines) of the samples. The difference between the
57 extrapolated data and the refined profile is shown under each curve. Supplementary peaks form the instrument are present
58 (Cu k_β and W)

59